Article

Structural and Elastic Behaviour of Sodalite $Na_8(Al_6Si_6O_{24})Cl_2$ at High-Pressure by First-Principle Simulations

Gianfranco Ulian * and **Giovanni Valdrè ***

Centro di Ricerche Interdisciplinari di Biomineralogia, Cristallografia e Biomateriali, Dipartimento di Scienze Biologiche, Geologiche e Ambientali, Università di Bologna "Alma Mater Studiorum", Piazza di Porta San Donato 1, 40126 Bologna, Italy

* Correspondence: gianfranco.ulian2@unibo.it (G.U.); giovanni.valdre@unibo.it (G.V.)

Abstract: Sodalite $Na_8(Al_6Si_6O_{24})Cl_2$ (space group $P\bar{4}3n$) is an important mineral belonging to the zeolite group, with several and manyfold fundamental and technological applications. Despite the interest in this mineral from different disciplines, very little is known regarding its high-pressure elastic properties. The present study aims at filling this knowledge gap, reporting the equation of state and the elastic moduli of sodalite calculated in a wide pressure range, from -6 GPa to 22 GPa. The results were obtained from Density Functional Theory simulations carried out with Gaussian-type basis sets and the well-known hybrid functional B3LYP. The DFT-D3 a posteriori correction to include the van der Waals interactions in the physical treatment of the mineral was also applied. The calculated equation of state parameters at 0 GPa and absolute zero (0 K), i.e., $K_0 = 70.15(7)$ GPa, $K' = 4.46(2)$ and $V_0 = 676.85(3)$ Å3 are in line with the properties derived from the stiffness tensor, and in agreement with the few experimental data reported in the literature. Sodalite was found mechanically unstable when compressed above 15.6 GPa.

Keywords: sodalite; zeolite group; equation of state; stiffness tensor; seismic wave velocities; DFT; B3LYP

1. Introduction

Zeolites are both natural and synthetic nanoporous crystalline aluminosilicates (framework silicates) that are frequently used in important chemical industry applications, such as catalysis, separation ("molecular sieves"), and ion exchange [1,2]. From the crystal chemistry perspective, zeolites are made of a network of corner-sharing TO_4 tetrahedra, where T = Si, Al, or other tetrahedrally coordinated atoms (see for instance [3]).

The present work focuses on sodalite, whose chemical formula is $Na_8(Al_6Si_6O_{24})Cl_2$ and cubic structure (space group $P\bar{4}3n$). As determined by different structural refinements over the past century [4–7], this mineral is characterized by a β-cage that is made of four-membered $(Al,Si)O_4$ rings on the (100) plane (see Figure 1a) linked together in six-membered rings along the [111] direction (Figure 1b), leading to the $(AlSiO_4)_6^{6-}$ framework. The negative charge (-6) induced by the Al^{3+}/Si^{4+} substitutions is balanced by two tetrahedral $(Na_4Cl)^{3+}$ clusters. The structure is highly symmetric, with just five atoms in the asymmetric unit, i.e., Cl (Wyckoff site 2a) in (0,0,0), Al (6d) in (1/4,0,1/2), Si (6c) in (1/4,1/2,0), Na (8e) in (x,x,x) and O (24i) in (x,y,z).

In addition, sodalite and the hydrated variant known as hydrosodalite $Na_6(AlSiO_4)_6·8H_2O$ [8] are among the possible mineral phases synthesized during geopolymerisation [9]. This process requires kaolinite or metakaolin precursors that provide SiO_2 and Al_2O_3 in ratio 2:1 and a strong basic solution (pH > 12.5) of sodium hydroxide (NaOH) that hydrolyses the silicon and aluminium oxides [10], as observed with several techniques, such as X-ray diffraction and scanning electron microscopy [11–13].
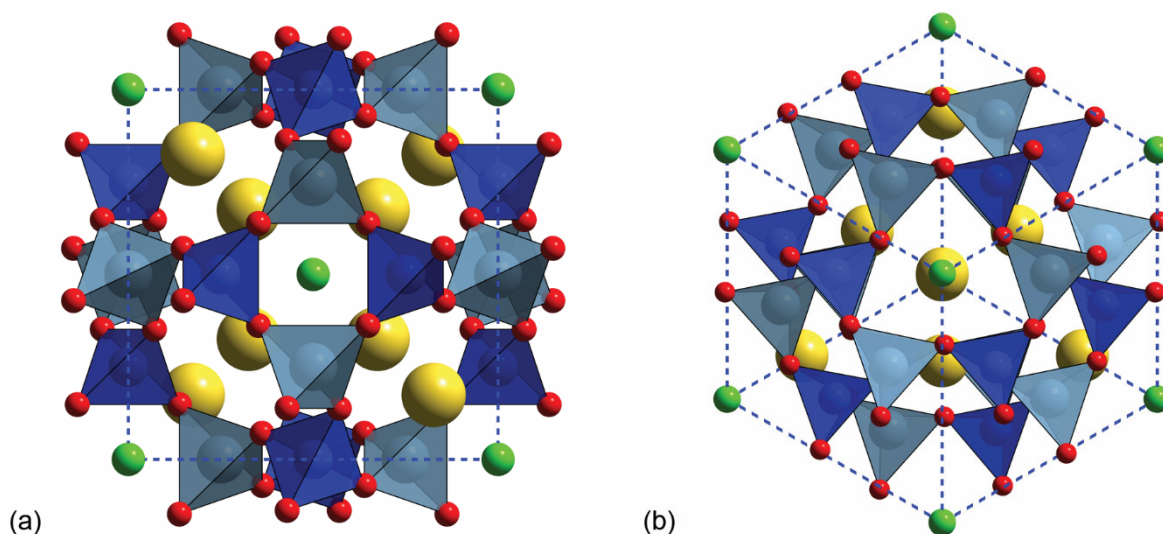
Figure 1. Sodalite $Na_8(Al_6Si_6O_{24})Cl_2$ polyhedral model seen along (**a**) the [100] and (**b**) the [111] directions. The dashed blue lines show the mineral lattice. Colour code for atoms: Blue—Si; cyan—Al; red—O; yellow—Na and green—Cl.

       Despite the diversified and multidisciplinary interest in sodalite, to the author's knowledge, only two experimental works addressed and investigated the elasticity of this mineral. Hazen and Sharp [14] reported the hydrostatic compression behaviour of a natural sodalite sample with composition $Na_{7.99}K_{0.01}(Al_{5.98}Fe_{0.04}Si_{5.98})O_{23.99}Cl_{1.96}(SO_4)_{0.02}$, from room to 2.6 GPa, but limited to the measurements of the unit cell volume and the *a* lattice parameter variations. No other works reported the equation of the state of sodalite at higher pressures. The second work is that of Li et al. [15], who provided the second-order elastic moduli of the mineral from ultrasound measurements. On the contrary, there have been several theoretical studies on sodalite, but they were mainly focused on the stoichiometric $Si_{12}O_{24}$ phase, which was selected as a prototype for framework silicates because of its simplicity [3,16]. The only available investigation on the elastic properties of sodalite with ideal formula $Na_8(Al_6Si_6O_{24})Cl_2$ is the theoretical one of Williams and co-workers [17], which was however conducted with classical mechanics methods (force fields). The knowledge of the elastic behaviour of sodalite is fundamental to assessing its mechanical stability, which ultimately affects the possible applications of this zeolite, for example in building materials (see geopolymers), water treatment, soil remediation, gas separation, and catalysis [18]. It is also worth remembering that sodalite and, in general, natural zeolites also occur as secondary minerals in several geological environments in the Earth's crust.

       The present work aims at filling these knowledge gaps, providing the readers with an ab initio analysis at the Density Functional Theory (DFT) level of the crystal chemistry and elastic properties of sodalite. Regarding the mechanical behaviour, the equation of state of the mineral up to about 22 GPa is here reported, investigating the effects of pressure on the internal geometry, i.e., bond distances and angles, and polyhedral volumes. Then, at each hydrostatically compressed state, the second-order elastic moduli were calculated and analysed to obtain other important properties, such as Young's and shear moduli, the compressibility, Poisson's ratio and the seismic wave velocities. This paper is organised as follows: after a brief description of the employed computational parameters (Section 2), the results related to the crystal chemistry, the equation of state and the elastic moduli (Section 3) will be presented and discussed against the few experimental and theoretical data available in the literature. Finally, some general conclusions will be presented in Section 4.

2. Computational Methods

The ab initio (DFT) simulations performed in the present study were carried out with the CRYSTAL17 code [19]. We selected the hybrid B3LYP functional [20,21] because it is known to provide structural, vibrational and elastic data that are in very good agreement with the experimental counterparts (see for instance [22–25]). The CRYSTAL code builds the multi-electronic wave function using the so-called linear combination of atomic orbitals (LCAO) approach, which employs Gaussian-type orbitals basis sets. Throughout the simulations, an 88-31G* [26], an 85-11G* [27] an 8-411d11G [28] an 8-511G [29] and an 86-311G [30] basis sets were employed to describe Si, Al, O, Na and Cl, respectively. They are double-ζ quality basis sets, i.e., they contain a double amount of Gaussian-type functions that describe the atomic orbitals, which ensure high accuracy with affordable computational costs. Furthermore, the basis sets for silicon, aluminium and oxygen were previously adopted for the simulations of the crystal chemical and elastic properties of other minerals, in particular talc [31], pyrophyllite [32,33], chlorite [34,35], topaz [36], brucite and portlandite [37].

The exchange–correlation contribution to the total energy is calculated within CRYSTAL code by numerical integration of the electron density and its gradient, a task performed on a pruned grid whose angular points are generated from the quadrature scheme of Gauss–Legendre, whereas the Lebedev approach is adopted to obtain the radial points [19]. The default grid of CRYSTAL17 was employed, which is made of 75 radial points and 974 angular points and represents a good compromise between accuracy and cost of calculation. The thresholds controlling the accuracy of the calculation of the Coulomb and exchange integrals were set to 10^{-8} (Coulomb series) and 10^{-16} (exchange series). The Hamiltonian matrix was diagonalized in 35 k points (reciprocal lattice points), corresponding to a shrinking factor of 8 [38]. To properly include the effects of long-range interactions in the simulations, typically neglected by both GGA and hybrid DFT functionals, we employed the DFT-D3 scheme proposed by Grimme and co-workers [39], which adds the following contribution term to the total energy of the system:

$$E_{DFT-D3} = -\frac{1}{2}\sum_{i=1}^{N}\sum_{j=1}^{N}\sum_{\mathbf{g}}\left[\frac{C_{6ij}}{r_{ij,\mathbf{g}}^6}f_{dump,6}\left(r_{ij,\mathbf{g}}\right) + \frac{C_{8ij}}{r_{ij,\mathbf{g}}^8}f_{dump,8}\left(r_{ij,\mathbf{g}}\right)\right] \tag{1}$$

The sums run over the atoms N in the unit cell, with $r_{ij,\mathbf{g}}$ the internuclear distance between atom i in cell $\mathbf{g} = 0$ (reference cell) and atom j in cell $\mathbf{g}$, and C_{nij} ($n = 6, 8$) terms are the 6th- and 8th-order dispersion coefficients for atom pairs ij, which depends on the geometry of the system. The damping function here adopted is the one proposed by Becke and Johnson [40–42]:

$$f_{dump,n}\left(r_{ij,\mathbf{g}}\right) = \frac{s_n r_{ij}^n}{r_{ij}^n + f\left(R_{0ij}\right)^n} \tag{2}$$

with $R_{0ij} = \sqrt{C_{8ij}/C_{6ij}}$ and $f\left(R_{0ij}\right) = \alpha_1 R_{0ij} + \alpha_2$, $s_6 = 1$, s_8, whereas α_1 and α_2 are adjustable parameters. The choice of including the long-range interactions is dictated by the need for the correct treatment of all the forces acting on the system because the elastic properties depend on their gradient (second derivatives of the energy with respect to the deformation). In fact, we observed that these weak forces play a non-negligible role even for those minerals and materials where long-range interactions are not predominant. We recently demonstrated this behaviour for calcite [43] and aragonite [44], and we expect the same for sodalite.

The lattice constants and the atomic coordinates were optimized within the same run with a numerical gradient method and an analytical gradient approach, respectively. The starting geometry used to create the sodalite model was taken from the experimental XRD refinements of Hassan and collaborators [4]. The upgrade of the Hessian matrix was performed by means of the well-known BFGS algorithm [45–49]. For the optimization of both the equilibrium (0 GPa) and hydrostatically compressed/expanded unit cell, the

tolerances for the maximum allowed gradient and the maximum atomic displacement for considering the geometry as converged have been set to 1×10^{-5} hartree bohr^{-1} and 4×10^{-5} bohr, respectively [50,51].

Second-order elastic moduli were calculated according to the scheme proposed by Perger and co-workers [52], which is implemented in the CRYSTAL code. The elastic moduli are the components of the 4th-rank stiffness tensor **C** that, according to the Voigt's 6×6 matrix representation, can be written as:

$$\sigma_v = C_{vu}\eta_u \tag{3}$$

where the indices v,u run from 1 to 6 (1 = xx, 2 = yy, 3 = zz, 4 = yz, 5 = xz and 6 = xy), σ_v and η_u are the components of the stress and pure strain second-rank tensors. The interested reader can find more information on the theory [53], implementation in the CRYSTAL code [52,54] and recent applications [36,37,51,55] in dedicated literature. Single-crystal elastic properties, namely Young's modulus (E), linear compressibility (β), shear modulus (μ) and Poisson's ratio (v) were calculated from the elastic moduli using the QUANTAS code [56], with well-known directional relations [34,53,55,57,58]. Voigt and Reuss equations were employed to calculate the average elastic properties considering the system as a polycrystalline aggregate as explained by Nye [53].

Graphical representations of the sodalite structure were made with the molecular graphics program VESTA [59].

3. Results

3.1. Crystal Chemistry

The crystal structure data (unit cell parameter a, atomic distances, bond angles, polyhedral volumes and relevant atomic fractional coordinates) of sodalite obtained from geometry optimization at equilibrium (0 K and 0 GPa) within the DFT/B3LYP-D3 approach is reported in Table 1, alongside previous theoretical [17] and experimental crystal chemical analyses [4–6].

Table 1. Zero-pressure (equilibrium) structure of sodalite $Na_8(Al_6Si_6O_{24})Cl_2$, with a the lattice parameter and V the unit cell volume, and internal geometry (atomic distances, bond angles, polyhedral volumes and relevant atomic fractional coordinates).

		B3LYP-D3	Δ	FF [1]	SR-XRPD [2]	ND [3]	XRD [4]
a (Å)		8.78091	−1.19%	8.848	8.88696	8.882	8.8823
V (Å^3)		677.0477	−3.54%	692.684	701.875	700.700	700.771
Si–O (Å)	(×4)	1.6298	0.60%	1.598	1.6201	1.620	1.620
Al–O (Å)	(×4)	1.7437	0.10%	1.758	1.7419	1.740	1.742
Na–O (Å)	(×3)	2.2750	−3.48%	2.316	2.357	2.354	2.353
Na–Cl (Å)	(×4)	2.6486	−2.52%	2.749	2.717	2.735	2.716
O–Si–O (°)	(×4)	107.53	0.06%	108.66	107.466	107.66	107.7
	(×2)	113.42	−0.12%	111.11	113.560	113.15	113.0
Mean		109.50	0.00%	109.48	109.50	109.49	109.47
O–Al–O (°)	(×4)	108.49	0.05%	109.88	108.442	108.62	108.7
	(×2)	111.45	−0.09%	108.66	111.550	111.18	111.0
Mean		109.48	0.00%	109.47	109.48	109.47	109.47
Si–O–Al (°)		133.90	−3.17%	137.49	138.288	138.24	
V_{SiO4} (Å^3)		2.2208	2.18%	2.0951	2.1734	2.1730	-
V_{AlO4} (Å^3)		2.7207	0.38%	2.7840	2.7103	2.7033	-
Na1 (8e)	x/a	0.17414	−2.11%	0.17937	0.1779	0.17780	0.1778
O1 (24i)	x/a	0.13816	−1.13%	0.13416	0.13974	0.13925	0.1390
	y/b	0.14813	−1.33%	0.14782	0.15013	0.14954	0.1494
	z/c	0.42940	−2.18%	0.43525	0.43895	0.43851	0.4383

Notes: Δ is the percentage difference between the B3LYP-D3 results and the experimental SR-XRPD refinements. [1]—Force field (FF) simulations [17]; [2]—synchrotron radiation X-ray powder diffraction (SR-XRPD) measurements [4]; [3]—neutron diffraction (ND) determination; [4]—X-ray diffraction.

As expected from static ab initio simulations carried out at 0 K and without including zero-point effects, the unit cell volume is about 3.5% smaller than that found from the refinements of the structural data collected from synchrotron radiation X-ray powder diffraction (SR-XRPD) of Hassan et al. [4]. By analysing the internal geometry, it is possible to note the interplay between the Si–O and Al–O bond lengths, slightly larger than the experimental ones (less than 1%), and the Na–O and Na–Cl distances, which are instead underestimated by about 3%. The mean O–Si–O and O–Al–O bond angles are in excellent agreement with the experimental ones, and very close to the ideal tetrahedral angle (109.47°) whereas the bridging Si–O–Al angle is slightly underestimated (about −3%). The bridging angle is the one that showed the greatest variation as a function of temperature, a behaviour that was modelled with a parabolic function in the range of 28–1000 °C in the work of Hassan and collaborators [4]. By extrapolating at 0 K (−273.15 °C) with the functional form proposed by the cited authors, we obtained a Si–O–Al angle of 137.47°, which is still larger than that at the B3LYP-D3 level. This could be due to the absence of any thermal effects, including zero-point energy, i.e., the ground-state vibrational contribution to the total internal energy, and the associated isotropic displacement parameters that were not taken into account in the present investigation. The volumes of the SiO_4 and AlO_4 tetrahedra are also in line with the XRD refinements. Our results are also in good agreement with the statistical data collected for hundreds of zeolites, including sodalite-like structures reported by Baur and Fischer [60]. The authors calculated a mean T–O bond distance of 1.617(7) Å (1.629 Å by applying a correction for bond distances) for SOD zeolites and observed O–Si–O and O–Al–O angles in the ranges 101.0°–117.7° and 94.6°–123.7°, respectively. Our simulations on stoichiometric sodalite provided both distances and angular values that fall in these ranges.

The present results at the DFT/B3LYP-D3 level of theory are in line with the force field (classical mechanics) simulations of Willams et al. [17], and provide a better mean absolute deviation of the structural features of sodalite (1.28%) in comparison to the cited work (1.49%). Unfortunately, despite recent ab initio studies on sodalite performed in the last decade [61–63], none of them reported the crystal chemistry of the optimized zeolite structure for a proper comparison, focusing on other properties of the mineral (electronic band structure and optical properties, spectroscopic models of localized defects in the structure, reactivity towards sulphur).

3.2. Equation of State

The equation of the state of sodalite was obtained with a two-step process. In the first one, it was performed a volume-constrained geometry optimization on a series of mineral unit cells with larger (expansion) and smaller (compression) volumes. Here, eleven models between $0.82 \cdot V_{eq}$ and $1.12 \cdot V_{eq}$, with V_{eq} the equilibrium unit cell volume, were simulated using the internal routines of CRYSTAL [54]. The geometry optimization results at different hydrostatic compression/expansion states are reported in Table 2.

Then, in the second step of the procedure, the unit cell internal energy as a function of volume, $U(V)$, was fitted to a volume-integrated 3rd-order Birch–Murnaghan (BM3) formulation [64], as proposed by Hebbache and Zemzemi [65]:

$$U(V) = U_0 + \frac{9}{16} K_0 V_0 \left\{ K\prime \left(X^2 - 1 \right)^3 + \left[\left(X^2 - 1 \right)^2 \left(6 - 4X^2 \right) \right] \right\} \tag{4}$$

with $X = (V_0/V)^{-1/3}$. In this equation, the fitting parameters are U_0 (internal energy), K_0 (bulk modulus), $K\prime$ (pressure derivative of the bulk modulus) and V_0 (unit cell volume), with the subscript zero meaning they were obtained at 0 GPa. This operation was performed using the QUANTAS code [56], obtaining $K_0 = 70.15(7)$ GPa, $K\prime = 4.46(2)$ and $V_0 = 676.85(3)$ $Å^3$. This result is in quite good agreement with that reported by Hazen and Sharp [14], with second-order Birch–Murnaghan equation of state fitting parameters $K_0 = 52(8)$ GPa and $K\prime = 4$ (fixed). The difference between the fitting results could be due to several reasons, the first one the absence of thermal effects in the simulations,

as previously introduced during the discussion of the sodalite crystal chemistry. Then, the composition of the experimental sample and the theoretical model is slightly different, because the former has some percentages of other elements [chemical formula $Na_{7.99}K_{0.01}(Al_{5.98}Fe_{0.04}Si_{5.98})O_{23.99}Cl_{1.96}(SO_4)_{0.02}$, as obtained from microprobe analysis], whereas the present DFT investigation considered an ideal, stoichiometric sodalite. Finally, the present study considered a very wide pressure range, up to about 22 GPa, whereas the high-pressure XRD refinements were carried out only up to 2.6 GPa, as can be noted from Figure 2a.

Table 2. Unit cell volume *V*, lattice parameter *a*, differences in internal energy (ΔU) and enthalpy (ΔH) with respect to the equilibrium geometry (0 GPa), mean bond lengths and angles, polyhedron volume of SiO_4 and AlO_4 tetrahedra and position of the sodium and oxygen atoms as a function of pressure.

| *P* (GPa)		22.4	17.2	12.8	9.0	5.7	2.9	0.5	0.0	−1.6	−3.4	−4.9	−6.3
a (Å)		8.21885	8.30886	8.39887	8.48889	8.57890	8.66891	8.75892	8.78091	8.84893	8.93895	9.02896	9.11897
V (Å³)		555.1791	573.6204	592.4656	611.7191	631.3853	651.4685	671.9731	677.0477	692.9035	714.2641	736.0593	758.2934
ΔU (Ha)		0.25216	0.17133	0.10779	0.06053	0.02783	0.00821	0.00029	0.00000	0.00293	0.01512	0.03580	0.06407
ΔH (Ha)		3.10532	2.43655	1.84532	1.32244	0.85921	0.44818	0.08293	0.00000	−0.24208	−0.53150	−0.78961	−1.02002
Si–O (Å)	(×4)	1.593	1.600	1.607	1.613	1.618	1.624	1.629	1.630	1.633	1.638	1.642	1.646
Al–O (Å)	(×4)	1.692	1.702	1.711	1.719	1.727	1.735	1.742	1.744	1.749	1.756	1.762	1.768
Na–O (Å)	(×3)	2.047	2.081	2.116	2.152	2.189	2.227	2.265	2.275	2.306	2.348	2.392	2.438
Na–Cl (Å)	(×4)	2.307	2.355	2.405	2.458	2.514	2.571	2.633	2.649	2.697	2.764	2.835	2.910
O–Si–O (°)	(×4)	107.51	107.53	107.52	107.52	107.52	107.52	107.53	107.53	107.54	107.55	107.57	107.59
	(×2)	113.46	113.44	113.45	113.46	113.45	113.44	113.43	113.42	113.41	113.38	113.34	113.30
Mean		109.50	109.50	109.50	109.50	109.50	109.50	109.50	109.50	109.50	109.50	109.49	109.49
O–Al–O (°)	(×4)	108.50	108.51	108.50	108.50	108.50	108.49	108.49	108.49	108.49	108.50	108.50	108.51
	(×2)	111.43	111.41	111.42	111.43	111.44	111.44	111.45	111.45	111.44	111.43	111.42	111.41
Mean		109.48	109.48	109.48	109.48	109.48	109.48	109.48	109.48	109.48	109.48	109.48	109.48
Si–O–Al (°)		124.34	125.62	127.01	128.49	129.94	131.71	133.46	133.90	135.30	137.25	139.34	141.56
V_{SiO4} (Å³)		2.0743	2.1018	2.1273	2.1513	2.1739	2.1956	2.216	2.2208	2.2354	2.2539	2.2714	2.2879
V_{AlO4} (Å³)		2.4868	2.5300	2.5698	2.6078	2.6442	2.6792	2.7127	2.7207	2.7454	2.7769	2.8069	2.8361
V_{Na4Cl} (Å³)		6.3022	6.6986	7.1392	7.6251	8.1519	8.7258	9.3685	9.5350	10.0683	10.8319	11.6879	12.6480
Na (8*e*)	*x/a*	0.16207	0.16361	0.16533	0.16720	0.16917	0.17126	0.17356	0.17414	0.17597	0.17850	0.18125	0.18425
O (24*i*)	*x/a*	0.13402	0.13458	0.13524	0.13592	0.13660	0.13729	0.13799	0.13816	0.13868	0.13937	0.14006	0.14075
	y/b	0.14366	0.14432	0.14505	0.14578	0.14651	0.14723	0.14796	0.14813	0.14867	0.14937	0.15008	0.15077
	z/c	0.40887	0.41163	0.41464	0.41783	0.42118	0.42472	0.42845	0.42940	0.43239	0.43657	0.44107	0.44591

(a)

(b)

(c)
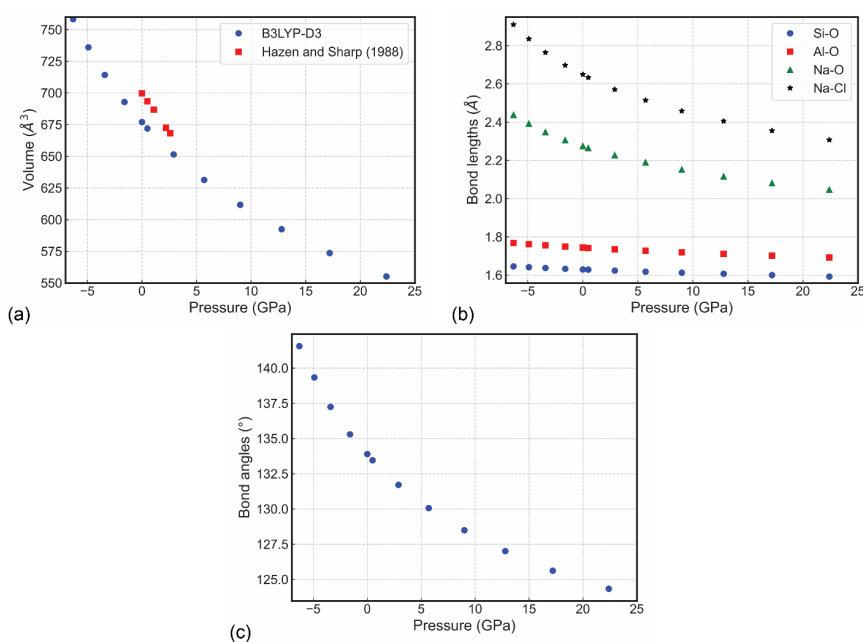
Figure 2. Sodalite (**a**) unit cell volume, (**b**) bond lengths and (**c**) Si–O–Al bridging angle variations as a function of pressure. In panel (**a**), the results of Hazen and Sharp [14] are reported for a direct comparison.

The bulk modulus calculated at the DFT level is also in line with the adiabatic bulk modulus ($K_S = 55.3$ GPa) calculated from the elastic moduli measured by ultrasonic methods by Li et al. [15]. To the authors' knowledge, no other theoretical and experimental data on the equation of state were reported in literature regarding sodalite with the ideal chemical formula [$Na_8(Al_6Si_6O_{24})Cl_2$] here reported. Albeit the different cage structure, the elastic behaviour of sodalite is in line with that of cancrinite-group zeolites as recently reviewed by Chukanov and co-workers [66], whose bulk moduli fall in the range 30–48 GPa.

An inspection of the variation of the internal geometry (Figure 2b,c and Table 2) provides more insights into the compression mechanism. The structural features that are affected the most by hydrostatic pressure are the Si–O–Al bridging angles (–7.1% at about 22 GPa with respect to the equilibrium geometry), the Na–O (–10.0%) and Na–Cl (–12.9%) bond distances and the Na_4Cl polyhedral volume (–33.9%). Conversely, the SiO_4 and AlO_4 bond lengths are just slightly affected by compression (up to about −3%), whereas the O–Si–O and O–Al–O angles remain constant. A graphical representation of the sodalite structure at the extremes of the compression regime investigated here is reported in Figure 3. All these observations agree with the general behaviour of framework silicates, such as zeolites and feldspathoids. Indeed, these minerals undergo a small distortion of the framework on the T–O–T angles, with more or less rigid T–O bonds, and high compression of the cation sites [14].
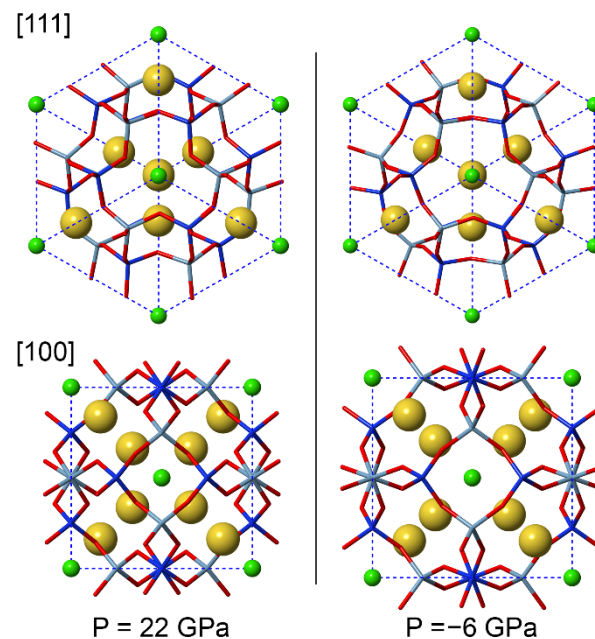

Figure 3. Sodalite framework at 22 GPa (**left**) and −6 GPa (**right**), as seen from the [111] and [100] directions. The wireframe structure is composed by Al (cyan), Si (blue) and O (red), whereas the Na and Cl atoms are shown as yellow and green spheres, respectively.

3.3. Elastic Moduli and their Variation with Pressure

Cubic crystals have three independent elastic moduli (C_{11}, C_{44} and C_{12}) that can be represented in a 6×6 matrix **C** using Voigt's notation [53]:

$$\mathbf{C} = \begin{pmatrix} C_{11} & C_{12} & C_{12} & \cdot & \cdot & \cdot \\ & C_{11} & C_{12} & \cdot & \cdot & \cdot \\ & & C_{11} & \cdot & \cdot & \cdot \\ & & & C_{44} & \cdot & \cdot \\ & & & & C_{44} & \cdot \\ & & & & & C_{44} \end{pmatrix} \quad (5)$$

where the dots indicate the C_{ij} value is zero. For symmetry reasons, two lattice deformations are sufficient to obtain all the independent elastic moduli:

$$\varepsilon_1 = \delta \begin{pmatrix} 1 & 0 & 0 \\ 0 & 0 & 0 \\ 0 & 0 & 0 \end{pmatrix} \tag{6}$$

and

$$\varepsilon_4 = \delta \begin{pmatrix} 0 & 0 & 0 \\ 0 & 0 & 1 \\ 0 & 1 & 0 \end{pmatrix} \tag{7}$$

with ε_1 and ε_4 being uniaxial and biaxial (shear) strains, respectively. The factor δ controls the amount of applied strain, which was varied between ± 0.015 with a step of 0.005, hence seven configurations for each lattice strain were simulated.

The calculated elastic moduli of sodalite in equilibrium conditions (0 K and 0 GPa) and by varying pressure are reported in Table 3, together with the polycrystalline properties calculated with the Voigt, Reuss and Hill averaging schemes. According to the Born criteria [67], a cubic crystalline structure is stable when the following necessary and sufficient conditions are met:

$$C_{11} - C_{12} > 0,\ C_{11} + 2C_{12} > 0,\ C_{44} > 0. \tag{8}$$

Table 3. Elastic moduli C_{ij} (GPa), density ρ (kg m^{-3}), bulk modulus (K, GPa), linear compressibility (β, TPa^{-1}), Young's modulus (E, GPa), shear modulus (μ, GPa), Poisson's ratio (v), and average longitudinal and shear wave velocities (v_P and v_S, respectively), of sodalite as a function of pressure P (GPa).

P	22.4 *	17.2 *	12.8	9.0	5.7	2.9	0.5	0.0	−1.6	−3.4	−4.9	−6.3
C_{11}	146.00	138.78	130.19	121.50	114.29	107.26	101.19	99.91	95.88	89.45	83.98	78.95
C_{44}	5.94	16.91	23.57	28.35	32.05	35.02	37.49	37.99	39.39	40.58	41.09	41.00
C_{12}	168.76	143.79	121.38	101.79	85.16	70.39	57.85	55.16	47.18	36.85	28.52	21.38
ρ	2894	2801	2712	2626	2544	2466	2391	2373	2319	2249	2183	2119
K	-	-	124.32	108.36	94.87	82.68	72.30	70.08	63.41	54.38	47.01	40.57
β	-	-	2.68	3.08	3.51	4.03	4.61	4.76	5.26	6.13	7.09	8.22
E_V	-	-	45.76	59.05	69.08	76.41	81.74	82.74	85.18	86.18	85.55	83.55
E_R	-	-	25.21	46.28	60.36	69.99	76.77	78.07	81.27	83.04	83.05	81.64
E_{VRH}	-	-	35.58	52.71	64.74	73.22	79.26	80.42	83.23	84.62	84.30	82.60
μ_V	-	-	15.90	20.95	25.05	28.39	31.16	31.75	33.38	34.87	35.74	36.12
μ_R	-	-	8.60	16.20	21.65	25.75	29.01	29.70	31.59	33.34	34.45	35.05
μ_{VRH}	-	-	12.25	18.57	23.35	28.07	30.09	30.72	32.48	34.10	35.09	35.58
v_V	-	-	0.439	0.409	0.379	0.346	0.312	0.303	0.276	0.236	0.197	0.157
v_R	-	-	0.466	0.429	0.394	0.359	0.323	0.314	0.286	0.245	0.206	0.165
v_{VRH}	-	-	0.452	0.419	0.386	0.352	0.317	0.309	0.281	0.241	0.201	0.161
v_S	-	-	2.125	2.660	3.030	3.313	3.547	3.598	3.743	3.894	4.010	4.098
v_P	-	-	7.202	7.120	7.038	6.940	6.857	6.841	6.784	6.663	6.555	6.445

Note: the bulk modulus values are the same between the three polycrystalline averaging schemes ($K_V = K_R = K_{VRH}$). The elastic properties were not calculated for the mechanically unstable sodalite models (marked with an asterisk).

The second and third criteria are satisfied throughout the pressure conditions explored in the present work. However, the first condition is not met at 17.2 GPa and 22.4 GPa (see Figure 4a) and, by fitting the data with a second-order polynomial, it was observed that the maximum allowed compression is about 15.6 GPa (black square in Figure 4a). Hence, it is expected that sodalite is not mechanically stable above this pressure threshold and it could undergo a phase transition or decomposition, according to our symmetry-constrained simulations at absolute zero.

The value of the bulk modulus at equilibrium geometry, $K_R = K_V = K_{VRH} = 70.08$ GPa, can be exploited to assess the quality of the simulation approach by comparing it to

the K_0 equation of state parameter. Since their difference is extremely low (0.1%), the computational methods here employed are consistent and physically valid.

Further positive assessment of the simulated stiffness components comes from the comparison with the experimental ones determined by Li and co-workers [15] with ultrasound techniques (C_{11} = 88.52 GPa C_{44} = 36.46 GPa and C_{12} = 38.72 GPa). In detail, the DFT/B3LYP-D3 results at zero temperature and pressure differ by about +13%, +4% and +42% for the C_{11}, C_{44} and C_{12} moduli, respectively, an observation in line with the equation of state previously discussed.
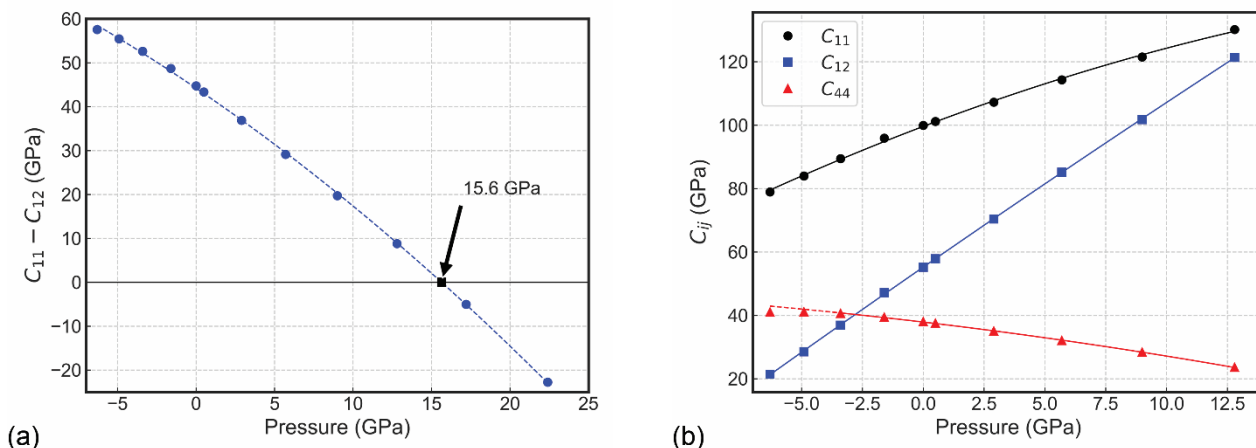
Figure 4. (**a**) Evolution of the mechanical stability criterion $C_{11} - C_{12} > 0$, with the black square showing the occurrence of instability above 15.6 GPa. (**b**) Elastic moduli of sodalite as a function of pressure, within the stability region. The lines are 2nd-order polynomial fit of the data (see text for details).

The graph showing the evolution of the elastic moduli with pressure is presented in Figure 4b, with the uniaxial components C_{11} and C_{12} increasing with P, whereas an inverse trend is observed for the shear component C_{44}. The functional description of the variation of the stiffness matrix with pressure was obtained for each $C_{ij}(P)$ curve by means of a finite strain fit of the type:

$$C_{ij}(P) = C_{ij0} + C_{ij}'P + C_{ij}''P^2 \tag{9}$$

where C_{ij0} is the elastic modulus value at zero pressure (in GPa units), C_{ij}' is the pressure derivative of C_{ij} (dC_{ij}/dP) is dimensionless and C_{ij}'' is the pressure second derivative of the elastic modulus (d^2C_{ij}/d^2P, in GPa^{-1} units). The regression of the data resulted in a_0 = 99.59 GPa, a_1 = 2.9102 and a_2 = −4.4238·10^{-2} GPa^{-1} for C_{11} (R^2 = 0.9988); a_0 = 37.86 GPa, a_1 = −0.9051 and a_2 = −1.6801·10^{-2} GPa^{-1} for C_{44} (R^2 = 0.9997); and a_0 = 55.19 GPa, a_1 = 5.3134 and a_2 = −1.1938·10^{-2} GPa^{-1} for C_{12} (R^2 = 0.9999). Hence, the rate of stiffening of the off-diagonal C_{12} modulus, i.e., C_{12}', is higher than that of the C_{11} term by about 1.8 times, explaining the mechanical instability previously discussed.

Finally, the wave velocities were calculated for single-crystal sodalite by solving the Christoffel's equation in the case a monochromatic plane wave with wave vector **q**, which is the propagation direction [68]:

$$\sum_{ij} \left[M_{ij} - \rho v_p^2 \delta_{ij} \right] s_j = 0, \tag{10}$$

where M_{ij} is a component of the Christoffel matrix M:

$$M_{ij} = \sum_{kl} q_k C_{iklj} q_l, \tag{11}$$

C_{ijkl} are the elastic moduli (in 4th-rank notation), ρ is the crystal density, v_p is the wave velocity (known as *phase velocity*), δ_{ij} is the Kronecker's delta function and **s** is the polarization. Since the velocities are independent of the wavelength, **q** is assumed as a dimensionless unit vector denoting only the direction of travel of a monochromatic plane wave. The solutions of Christoffel's equation above reported are one primary (P-wave, longitudinal, v_{P}) and two secondary (S-wave, transverse, v_{S}) acoustic wave velocities, with the eigenvectors describing the polarization directions. However, since sound waves are never purely monochromatic, it is more realistic to calculate the so-called group velocities, v_g, which consider the sound as a wave packet with a small spread in wavelength and direction of travel, according to the formula [69]:

$$\mathbf{v}_g = \vec{\nabla} v_p \tag{12}$$

The gradient of the phase velocities is a derivative to the components of **q**, which is calculated in the reciprocal space (assumed dimensionless). It is worth noting that, while v_p is a scalar function of **q**, $\mathbf{v}_g$ is a vector that is not necessarily parallel to **q**, and the angle between the two velocities (phase and group) is given by

$$v_p = v_g \cos \psi \tag{13}$$

with ψ being called the power flow angle. The power flow angle varies as a function of the direction because **q** and $\mathbf{v}_g$ are not parallel, thus there are some directions showing concentration of the energy flux, whereas others are characterized by its dispersion. This effect, also known as the phonon focusing effect, is quantified by the enhancement factor A [70]:

$$A = \frac{\Delta\Theta_p}{\Delta\Theta_g}, \tag{14}$$

where $\Delta\Theta_p$ and $\Delta\Theta_g$ are defined as the solid angles that are crossed phase wave vectors $\mathbf{n}_p$ and group wave vectors $\mathbf{n}_g$, respectively. $\mathbf{n}_p$ and $\mathbf{n}_g$ are the normalized vectors of the phase and group velocities, respectively. More details can be found in the dedicated literature [69–71].

The seismic velocity results, i.e., phase velocity v_p, group velocity v_g, enhancement factor A and power flow angle ψ for sodalite at 0 GPa are reported in Figure 5, as upper hemisphere (Z > 0) Lambert equal-area projections on the XY plane. The cubic symmetry of the mineral is immediately recognizable from the patterns in each panel and for longitudinal and transverse acoustic waves. The enhancement factor is different according to the type of wave. For the P-mode, A is lowest along the Cartesian [100], [010] and [001] directions (Cartesian X, Y and Z) and the highest along the [111] direction. While the distribution of the enhancement factor is simple for P-waves, when considering the transverse modes there are complex patterns, with the lowest A value along the [111] direction.

By increasing pressure, the phase velocities change their minimum–maximum value ranges, but their directional distribution is almost unvaried, as shown in Figure 6 relatively to the mineral compressed at 12.8 GPa. However, there are striking differences in the group velocities v_g, especially for the slow and fast S-waves (Figure 6b), maintaining the cubic symmetry. These variations are due to the power flow angle values increasing up to about 70° (slow waves) and 45° (fast waves) at the maximum pressure investigated (12.8 GPa), whereas they were much lower (30° and 20°, respectively), at 0 GPa. Conversely, primary waves are less affected by pressure effects. The enhancement factor A clearly shows higher variations of the power flow angle, as reported in the logarithmic plots in Figures 5c and 6c.
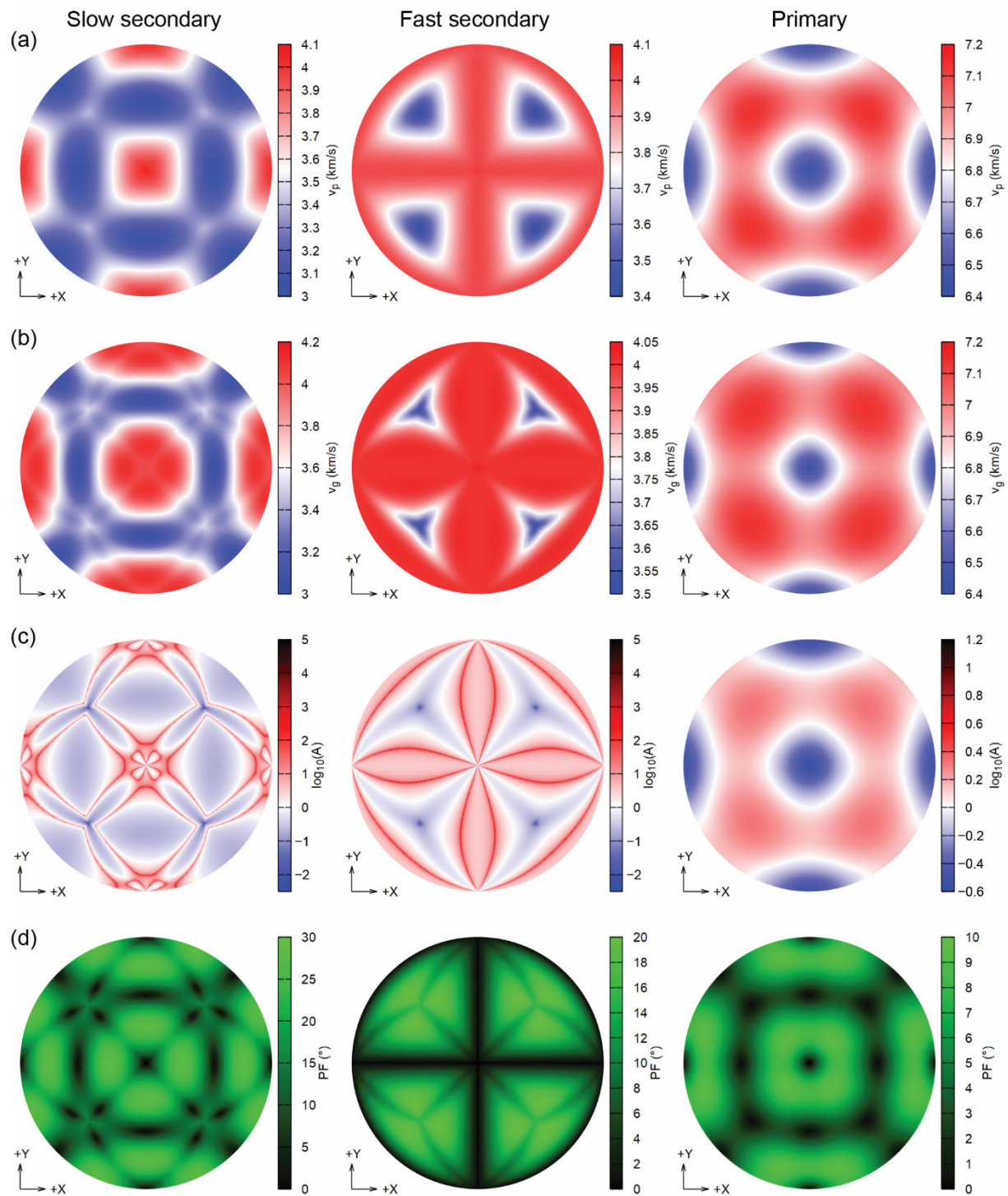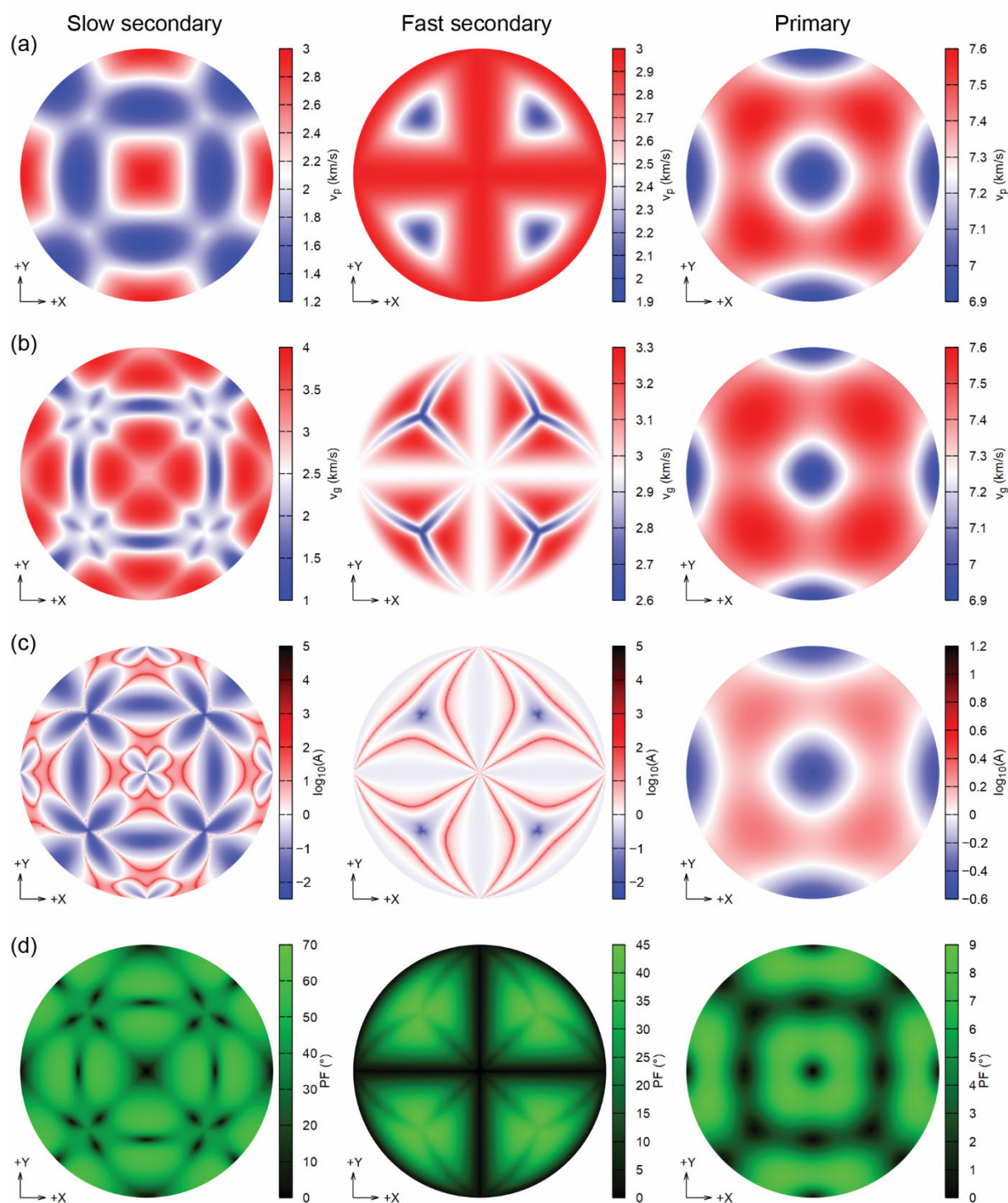
Figure 5. Analysis of the seismic wave velocities (Lambert equal-area upper hemisphere projections) of sodalite at 0 GPa, showing (**a**) the phase velocities v_P (km/s), (**b**) the group velocities v_P (km/s), (**c**) the enhancement factor A and (**d**) the power flow angle (PF, °).

Figure 6. Analysis of the seismic wave velocities (Lambert equal-area upper hemisphere projections) of sodalite at 12.8 GPa, showing (**a**) the phase velocities v_P (km/s), (**b**) the group velocities v_P (km/s), (**c**) the enhancement factor A and (**d**) the power flow angle (PF, °).

4. Conclusions

In the present work, we provided for the first time an ab initio investigation of the crystal chemical and elastic properties of sodalite [$Na_8(Al_6Si_6O_{24})Cl_2$, space group $P\bar{4}3n$], a zeolite mineral with important fundamental (geological and minero-petrographic) and technological (e.g., catalysis and separation, building and construction materials) applications. The knowledge of the elastic behaviour of this mineral under pressure is important

to assess its mechanical stability and guide the possible use of the material in specific applications. The study was conducted at the Density Functional Theory level, using the well-known hybrid functional B3LYP corrected with the DFT-D3 scheme to include the contributions arising from van der Waals interactions.

Albeit being at absolute zero (0 K), the third-order Birch–Murnaghan equation of the state of the mineral calculated from the $U(V)$ curves up to about 22 GPa is in line with the few experimental studies reported in the literature. The analysis of the internal geometry showed that the compression mechanism is controlled by both the Na–O and Na–Cl distances, and hence on the respective tetrahedral volumes, and the T–O–T bridging angle. Conversely, the aluminosilicate framework, i.e., the Si–O and Al–O bonds, was the least affected by pressure. No sign of abrupt structural variations in the considered hydrostatic pressure range suggested a possible phase transition or decomposition. However, it must be recalled that the simulations were conducted by constraining the symmetry, thus the unit cell and its atoms were free to relax within the symmetry operations of the $P\bar{4}3n$ space group. In fact, from the elastic point of view, the necessary and sufficient Born stability criteria were not satisfied above 15.6 GPa, meaning that sodalite is not mechanically stable above this pressure threshold. In future, high-pressure simulations and thermodynamic analyses will be performed to check if other possible, more energetically favourable crystal structures exist.

Finally, the second-order elastic moduli of sodalite and their functional variation with pressure were reported, information of utmost relevance for both geophysical studies and applications of the zeolite. The variation of the elastic moduli is well described by a finite-strain fit using second-order polynomial functions. In addition, single-crystal and polycrystalline elastic properties derived from the stiffness tensor were calculated as a reference for future studies on this mineral phase.

Author Contributions: Conceptualization, G.U. and G.V.; methodology, G.U.; validation, G.U. and G.V.; formal analysis, G.U.; investigation, G.U. and G.V.; data curation, G.U.; writing—review and editing, G.U. and G.V.; visualization, G.U.; supervision, G.V. All authors have read and agreed to the published version of the manuscript.

Institutional Review Board Statement: Not applicable.

Informed Consent Statement: Not applicable.

Data Availability Statement: Data are available within the present article.

Conflicts of Interest: The authors declare no conflict of interest.

References

1. Barrer, R.M. *Hydrothermal Chemistry of Zeolites*; Academic Press: London, UK; New York, NY, USA, 1982; p. 360.
2. Auerbach, S.M.; Carrado, K.A.; Dutta, P.K. *Handbook of Zeolite Science and Technology*; CRC Press: New York, NY, USA, 2003.
3. Astala, R.; Auerbach, S.M.; Monson, P.A. Density functional theory study of silica zeolite structures: Stabilities and mechanical properties of SOD, LTA, CHA, MOR, and MFI. *J. Phys. Chem. B* **2004**, *108*, 9208–9215. [CrossRef]
4. Hassan, I.; Antao, S.M.; Parise, J.B. Sodalite: High-temperature structures obtained from synchrotron radiation and Rietveld refinements. *Am. Miner.* **2004**, *89*, 359–364. [CrossRef]
5. Hassan, I.; Grundy, H.D. The crystal structures of sodalite-group minerals. *Acta Crystallogr. Sect. B Struct. Sci.* **1984**, *B40*, 6–13. [CrossRef]
6. McMullan, R.K.; Ghose, S.; Haga, N.; Schomaker, V. Sodalite, $Na_4Si_3Al_3O_{12}Cl$: Structure and ionic mobility at high temperatures by neutron diffraction. *Acta Crystallogr. Sect. B Struct. Sci.* **1996**, *52*, 616–627. [CrossRef]
7. Pauling, L. The structure of sodalite and helvite. *Z. Kristallogr.* **1930**, *74*, 213–225. [CrossRef]
8. Felsche, J.; Luger, S.; Baerlocher, C. Crystal structures of the hydro-sodalite $Na_6[AlSiO_4]_6$ $8H_2O$ and of the anhydrous sodalite $Na_6[AlSiO_4]_6$. *Zeolites* **1986**, *6*, 367–372. [CrossRef]
9. Davidovits, J. *Geopolymers Chemistry and Applications*, 5th ed.; Institute Géopolymère: Saint-Quentin, France, 2020.
10. Nagy, K.L.; Blum, A.E.; Lasaga, A.C. Dissolution and precipitation kinetics of kaolinite at 80 degrees C and pH 3; The dependence on solution saturation state. *Am. J. Sci.* **1991**, *291*, 649–686. [CrossRef]

11. Armigliato, A.; Valdré, G. Analytical electron microscopy of Al/TiN contacts on silicon for applications to very large scale integrated devices. *J. Appl. Phys.* **1987**, *61*, 390–396. [CrossRef]

12. Burciaga-Díaz, O.; Escalante-García, J.I. Structural transition to well-ordered phases of NaOH-activated slag-metakaolin cements aged by 6 years. *Cem. Concr. Res.* **2022**, *156*, 106791. [CrossRef]

13. Gatti, A.M.; Valdrè, G.; Tombesi, A. Importance of microanalysis in understanding mechanism of transformation in active glassy biomaterials. *J. Biomed. Mater. Res.* **1996**, *31*, 475–480. [CrossRef]

14. Hazen, R.M.; Sharp, Z.D. Compressibility of sodalite and scapolite. *Am. Mineral.* **1988**, *73*, 1120–1122.

15. Li, Z.; Nevitt, M.V.; Ghose, S. Elastic constants of sodalite $Na_4Al_3Si_3O_{12}Cl$. *Appl. Phys. Lett.* **1989**, *55*, 1730–1731. [CrossRef]

16. Sangthong, W.; Limtrakul, J.; Illas, F.; Bromley, S.T. Stable nanoporous alkali halide polymorphs: A first principles bottom-up study. *J. Mater. Chem.* **2008**, *18*, 5871–5879. [CrossRef]

17. Williams, J.J.; Evans, K.E.; Walton, R.I. On the elastic constants of the zeolite chlorosodalite. *Appl. Phys. Lett.* **2006**, *88*, 021914. [CrossRef]

18. Gatta, G.D.; Lee, Y. Zeolites at high pressure: A review. *Miner. Mag.* **2014**, *78*, 267–291. [CrossRef]

19. Dovesi, R.; Erba, A.; Orlando, R.; Zicovich-Wilson, C.M.; Civalleri, B.; Maschio, L.; Rerat, M.; Casassa, S.; Baima, J.; Salustro, S.; et al. Quantum-mechanical condensed matter simulations with CRYSTAL. *Wires Comput. Mol. Sci.* **2018**, *8*, e1360. [CrossRef]

20. Becke, A.D. Density-Functional Thermochemistry. III. The Role of Exact Exchange. *J. Chem. Phys.* **1993**, *98*, 5648. [CrossRef]

21. Lee, C.; Yang, W.; Parr, R.G. Development of the Colle-Salvetti Correlation-Energy Formula into a Functional of the Electron-Density. *Phys. Rev. B* **1988**, *37*, 785–789. [CrossRef]

22. Prencipe, M.; Pascale, F.; Zicovich-Wilson, C.M.; Saunders, V.R.; Orlando, R.; Dovesi, R. The vibrational spectrum of calcite $(CaCO_3)$: An ab initio quantum-mechanical calculation. *Phys. Chem. Miner.* **2004**, *31*, 559–564. [CrossRef]

23. Ulian, G.; Moro, D.; Valdrè, G. Thermodynamic, elastic, and vibrational (IR/Raman) behavior of mixed type-AB carbonated hydroxylapatite by density functional theory. *Am. Miner.* **2021**, *106*, 1928–1939. [CrossRef]

24. Ulian, G.; Valdrè, G. Thermomechanical, electronic and thermodynamic properties of ZnS cubic polymorphs: An *ab initio* investigation on the zinc-blende—Rock-salt phase transition. *Acta Crystallogr. Sect. B Struct. Sci.* **2019**, *75*, 1042–1059. [CrossRef]

25. Pascale, F.; Zicovich-Wilson, C.M.; Orlando, R.; Roetti, C.; Ugliengo, P.; Dovesi, R. Vibration frequencies of $Mg_3Al_2Si_3O_{12}$ pyrope. An ab initio study with the CRYSTAL code. *J. Phys. Chem. B* **2005**, *109*, 6146–6152. [CrossRef] [PubMed]

26. Nada, R.; Nicholas, J.B.; McCarthy, M.I.; Hess, A.C. Basis sets for ab initio periodic Hartree-Fock studies of zeolite/adsorbate interactions: He, Ne, and Ar in silica sodalite. *Int. J. Quantum Chem.* **1996**, *60*, 809–820. [CrossRef]

27. Catti, M.; Valerio, G.; Dovesi, R.; Causà, M. Quantum-mechanical calculation of the solid-state equilibrium $MgO+\alpha$-$Al_2O_3 \leftrightarrows MgAl_2O_4$ (spinel) versus pressure. *Phys. Rev. B* **1994**, *49*, 14179–14187. [CrossRef] [PubMed]

28. Valenzano, L.; Torres, F.J.; Doll, K.; Pascale, F.; Zicovich-Wilson, C.M.; Dovesi, R. Ab initio study of the vibrational spectrum and related properties of crystalline compounds; the case of $CaCO_3$ calcite. *Z Phys. Chem.* **2006**, *220*, 893–912. [CrossRef]

29. Dovesi, R.; Roetti, C.; Freyria Fava, C.; Prencipe, M.; Saunders, V.R. On the elastic properties of lithium, sodium and potassium oxide. An ab initio study. *Chem. Phys.* **1991**, *156*, 11–19. [CrossRef]

30. Aprà, E.; Causa, M.; Prencipe, M.; Dovesi, R.; Saunders, V.R. On the structural properties of NaCl: An ab initio study of the B1-B2 phase transition. *J. Phys. Condens. Matter* **1993**, *5*, 2969–2976. [CrossRef]

31. Ulian, G.; Valdrè, G. Density functional investigation of the thermophysical and thermochemical properties of talc $[Mg_3Si_4O_{10}(OH)_2]$. *Phys. Chem. Miner.* **2015**, *42*, 151–162. [CrossRef]

32. Ulian, G.; Valdrè, G. Structural, vibrational and thermophysical properties of pyrophyllite by semi-empirical density functional modelling. *Phys. Chem. Miner.* **2015**, *42*, 609–627. [CrossRef]

33. Gatta, G.D.; Lotti, P.; Merlini, M.; Liermann, H.-P.; Lausi, A.; Valdrè, G.; Pavese, A. Elastic behaviour and phase stability of pyrophyllite and talc at high pressure and temperature. *Phys. Chem. Miner.* **2015**, *42*, 309–318. [CrossRef]

34. Ulian, G.; Moro, D.; Valdrè, G. First principle investigation of the mechanical properties of natural layered nanocomposite: Clinochlore as a model system for heterodesmic structures. *Compos. Struct.* **2018**, *202*, 551–558. [CrossRef]

35. Ulian, G.; Moro, D.; Valdrè, G. Infrared and Raman spectroscopic features of clinochlore Mg6Si4O10(OH)8: A density functional theory contribution. *Appl. Clay Sci.* **2020**, *197*, 105779. [CrossRef]

36. Ulian, G.; Valdrè, G. Effects of fluorine content on the elastic behavior of topaz $[Al_2SiO_4(F,OH)_2]$. *Am. Miner.* **2017**, *102*, 347–356. [CrossRef]

37. Ulian, G.; Valdrè, G. Equation of state and second-order elastic constants of portlandite $Ca(OH)_2$ and brucite $Mg(OH)_2$. *Phys. Chem. Miner.* **2019**, *46*, 101–117. [CrossRef]

38. Monkhorst, H.J.; Pack, J.D. Special points for Brillouin-zone integrations. *Phys. Rev. B* **1976**, *13*, 5188. [CrossRef]

39. Grimme, S.; Antony, J.; Ehrlich, S.; Krieg, H. A consistent and accurate ab initio parametrization of density functional dispersion correction (DFT-D) for the 94 elements H-Pu. *J. Chem. Phys.* **2010**, *132*, 154104. [CrossRef]

40. Becke, A.D.; Johnson, E.R. A density-functional model of the dispersion interaction. *J. Chem. Phys.* **2005**, *123*, 154101. [CrossRef]

41. Johnson, E.R.; Becke, A.D. A post-Hartree-Fock model of intermolecular interactions. *J. Chem. Phys.* **2005**, *123*, 024101. [CrossRef]

42. Johnson, E.R.; Becke, A.D. A post-Hartree-Fock model of intermolecular interactions: Inclusion of higher-order corrections. *J. Chem. Phys.* **2006**, *124*, 174104. [CrossRef]

43. Ulian, G.; Valdrè, G. Study of the variation of the optical properties of calcite with applied stress, useful for specific rock and material mechanics. *Sci. Rep.* **2022**, *12*, 299. [CrossRef]
44. Ulian, G.; Valdrè, G. Structural and elastic behaviour of aragonite at high-pressure: A contribution from first-principle simulations. *Comput. Mater. Sci.* **2022**, *212*, 111600. [CrossRef]
45. Broyden, C.G. The convergence of a class of double-rank minimization algorithms: 2. The new algorithm. *IMA J. Appl. Math.* **1970**, *6*, 222–231. [CrossRef]
46. Broyden, C.G. The convergence of a class of double-rank minimization algorithms: 1. General considerations. *IMA J. Appl. Math.* **1970**, *6*, 76–90. [CrossRef]
47. Fletcher, R. A new approach to variable metric algorithms. *Comput. J.* **1970**, *13*, 317–322. [CrossRef]
48. Goldfarb, D. A family of variable-metric methods derived by variational means. *Math. Comput.* **1970**, *24*, 23–26. [CrossRef]
49. Shanno, D.F. Conditioning of quasi-Newton methods for function minimization. *Math. Comput.* **1970**, *24*, 647–656. [CrossRef]
50. Ulian, G.; Moro, D.; Valdrè, G. Benchmarking dispersion-corrected DFT methods for the evaluation of materials with anisotropic properties: Structural, electronic, dielectric, optical and vibrational analysis of calcite ($CaCO_3$, space group: R_3c). *Phys. Chem. Chem. Phys.* **2021**, *23*, 18899–18907. [CrossRef]
51. Ulian, G.; Moro, D.; Valdrè, G. Elastic properties of heterodesmic composite structures: The case of calcite CaCO3 (space group $R\overline{3}c$). *Compos. Part C Open Access* **2021**, *6*, 100184. [CrossRef]
52. Perger, W.F.; Criswell, J.; Civalleri, B.; Dovesi, R. Ab-initio calculation of elastic constants of crystalline systems with the CRYSTAL code. *Comput. Phys. Commun.* **2009**, *180*, 1753–1759. [CrossRef]
53. Nye, J.F. *Physical Properties of Crystals*; Oxford University Press: Oxford, UK, 1957.
54. Erba, A.; Mahmoud, A.; Belmonte, D.; Dovesi, R. High pressure elastic properties of minerals from ab initio simulations: The case of pyrope, grossular and andradite silicate garnets. *J. Chem. Phys.* **2014**, *140*, 124703. [CrossRef]
55. Ulian, G.; Valdrè, G. Second-order elastic constants of hexagonal hydroxylapatite ($P6_3$) from ab initio quantum mechanics: Comparison between DFT functionals and basis sets. *Int. J. Quantum Chem.* **2018**, *118*, e25500. [CrossRef]
56. Ulian, G.; Valdrè, G. QUANTAS: A Python software for the analysis of thermodynamics and elastic behavior of solids from ab initio quantum mechanical simulations and experimental data. *J. Appl. Crystallogr.* **2022**, *55*, 386–396. [CrossRef] [PubMed]
57. Marmier, A.; Lethbridge, Z.A.D.; Walton, R.I.; Smith, C.W.; Parker, S.C.; Evans, K.E. ElAM: A computer program for the analysis and representation of anisotropic elastic properties. *Comput. Phys. Commun.* **2010**, *181*, 2102–2115. [CrossRef]
58. Gaillac, R.; Pullumbi, P.; Coudert, F.X. ELATE: An open-source online application for analysis and visualization of elastic tensors. *J. Phys. Condens. Matter* **2016**, *28*, 275201. [CrossRef]
59. Momma, K.; Izumi, F. VESTA: A three-dimensional visualization system for electronic and structural analysis. *J. Appl. Crystallogr.* **2008**, *41*, 653–658. [CrossRef]
60. Baur, W.H.; Fischer, R.X. The Floppiness of It All: Bond Lengths Change with Atomic Displacement Parameters and the Flexibility of Various Coordination Tetrahedra in Zeolitic Frameworks. An Empirical Structural Study of Bond Lengths and Angles. *Chem. Mater.* **2019**, *31*, 2401–2420. [CrossRef]
61. Cano, N.F.; Ayta, W.E.F.; Watanabe, S. The electronic and optical properties of sodalite (Na8 Al6 Si6 O24 Cl2) from first principles. *Solid State Commun.* **2010**, *150*, 195–197. [CrossRef]
62. Colinet, P.; Gheeraert, A.; Curutchet, A.; Le Bahers, T. On the Spectroscopic Modeling of Localized Defects in Sodalites by TD-DFT. *J. Phys. Chem. C* **2020**, *124*, 8949–8957. [CrossRef]
63. Stoliaroff, A.; Schira, R.; Blumentritt, F.; Fritsch, E.; Jobic, S.; Latouche, C. Point Defects Modeling Explains Multiple Sulfur Species in Sulfur-Doped Na4(Al3Si3O12)Cl Sodalite. *J. Phys. Chem. C* **2021**, *125*, 16674–16680. [CrossRef]
64. Birch, F. Finite elastic strain of cubic crystals. *Phys. Rev.* **1947**, *71*, 809. [CrossRef]
65. Hebbache, M.; Zemzemi, M. Ab initio study of high-pressure behavior of a low compressibility metal and a hard material: Osmium and diamond. *Phys. Rev. B* **2004**, *70*, 224107. [CrossRef]
66. Chukanov, N.V.; Aksenov, S.M.; Rastsvetaeva, R.K. Structural chemistry, IR spectroscopy, properties, and genesis of natural and synthetic microporous cancrinite- and sodalite-related materials: A review. *Microporous Mesoporous Mater.* **2021**, *323*, 111098. [CrossRef]
67. Born, M.; Huang, K. *Dynamical Theory of Crystal Lattices*; Clarendon Press: Oxford, UK, 1954.
68. Musgrave, M.J.P. *Crystal Acoustics: Introduction to the Study of Elastic Waves and Vibrations in Crystals*; Holden-Day: San Francisco, CA, USA, 1970.
69. Jaeken, J.W.; Cottenier, S. Solving the Christoffel equation: Phase and group velocities. *Comput. Phys. Commun.* **2016**, *207*, 445–451. [CrossRef]
70. Muñoz-Santiburcio, D.; Hernández-Laguna, A.; Soto, J.I. AWESoMe: A code for the calculation of phase and group velocities of acoustic waves in homogeneous solids. *Comput. Phys. Commun.* **2015**, *192*, 272–277. [CrossRef]
71. Muñoz-Santiburcio, D.; Hernández-Laguna, A. AWESOME 1.1: A code for the calculation of phase and group velocities of acoustic waves in homogeneous solids. *Comput. Phys. Commun.* **2017**, *217*, 212–214. [CrossRef]